Electronic Supplementary Material (ESI) for Journal of Materials Chemistry C.

Two-dimensional Lead-free Perovskite $Cs_3Bi_2I_{8.3}Br_{0.7}$ Single Crystals with Anisotropic Ion Migration and Hard X-ray Response

Xiang Li, Guodong Zhang,* Yunqiu Hua, Xue Sun, Jiaxin Liu, Hongjie Liu, Zhongjie Yue, Zhongjun Zhai, Haibing Xia, and Xutang Tao*

State Key Laboratory of Crystal Materials, Institute of Crystal Materials, Shandong University, Jinan 250100, P. R. China;

Email: zgd@sdu.edu.cn; txt@sdu.edu.cn

1. Material characterization

XRD patterns were recorded using a Bruker-AXS D8 ADVANCE X-ray diffractometer (Bruker, Massachusetts, USA) in the range of 10°–90° (2θ) with a step size of 0.02° and scanning speed of 0.04 s step^{-1}. $Cs_3Bi_2I_{9-n}Br_n$ (CBIB) SCs were oriented using a Laue diffractometer (MULTIWIRE LABORATORIES 120, New Jersey, USA). The SEM and EDS measurements were performed using a field emission scanning electron microscope (S-4800, Hitachi, Tokyo, Japan) with energy dispersive X-ray spectrometry (EMAX Energy EX-350, Horiba, Kyoto, Japan). The UV-vis absorption spectroscopy was conducted using a Shimadzu UV-2550 spectrophotometer (Shimadzu, Kyoto, Japan) in the visible range. $BaSO_4$ was used as the reference sample. The $Cs_3Bi_2I_{8.3}Br_{0.7}$, $Cs_3Bi_2I_{8.5}Br_{0.5}$, and $Cs_3Bi_2I_9$ powders were placed on $BaSO_4$ powders, and they were pressed flat, then they were placed in the Shimadzu UV-2550 spectrophotometer for measuring. The hardness of the $(\bar{1}20)$ and (001) planes was performed by XHV-1000T micro-Vickers hardness apparatus furnished with a diamond square-based pyramid indenter. The specific heat was measured using a simultaneous thermal analyzer (TGA/DSC1/1600HT, Mettler-Toledo Inc.). The thermal diffusivity was measured via the laser flash method by using a laser flash apparatus (NETZSCH LFA 457 Nanoflash) in the temperature range of 25-200 °C. The thermal expansion was measured to a temperature of up to 300 °C using a thermal dilatometer (Diamond TMA, Perkin-Elmer Company). The Au electrodes were fabricated using ETD 3000 (Boyuan, Beijing, China). An electrometer (6517B, Keithley instruments, Ohio, USA) was used to apply bias voltage on SCs and record the response and dark current. The radiation dose rates of the sensitivity and low detection limit were carefully calibrated using a PIRANHA655 (Piranha, Sweden) and FLUKE451 (Danaher Corporation, USA) radiation detectors by adjusting the current of the tube, respectively. For photoconductivity measurement, X-ray was used as the illumination light.

2. X-ray response measurement.

To evaluate the X-ray detection performance, a tungsten target X-ray tube (RAD-14/leo, 32 kW-77 kW, Wuxi, China) was used as the source. The X-ray source was operated with a constant acceleration voltage of 40 and 100 keV. The dose rate was adjusted by changing the X-ray tube current from 10 to 25 mA in **Table S4-5**. The devices based on $Cs_3Bi_2I_{8.3}Br_{0.7}$ SC was placed in a dark shielding box to prevent ambient light interference. All the measurements were performed at room temperature (30 °C) in air.

3. The powder XRD patterns of $CBI_{8.3}Br_{0.7}$, $CBI_{8.5}Br_{0.5}$, and CBI SCs.

A ~16 g sample of high-purity 5N CsI: BiI_3 or CsBr: $BiBr_3$ (mole ratio of 3:2), purchased from Aladdin Chemistry Co. Ltd., was loaded into a silica ampoule evacuated to 1×10^{-5} Pa and sealed with an oxyhydrogen flame. The $CBI_{8.3}Br_{0.7}$ and $CBI_{8.5}Br_{0.5}$ were synthesized by CBI and CBB according to the stoichiometric ratio. Subsequently, the sealed ampoule was transferred to a well furnace that was controlled using a temperature controller (FP23, Shimaden, Tokyo, Japan). The well furnace was gradually heated to 660 °C at a rate of 45-55 °C h^{-1}. After maintaining temperature at 660 °C for 40 h, the well furnace was gradually cooled down to 30 °C at a rate of 15-25 °C h^{-1}. As shown in **Figure S1**, the powder XRD pattern of the polycrystalline $CBI_{8.3}Br_{0.7}$, $CBI_{8.5}Br_{0.5}$, and CBI were consistent with the simulated pattern based on SC data.

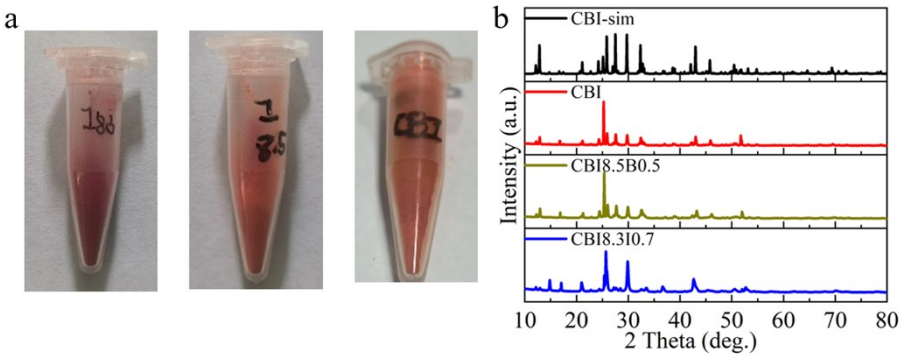

Figure S1. (a) Photographs and (b) Powder XRD patterns of CBIB SCs.

4. CBIB SC growth.

The synthesized polycrystalline CBIB, with diameters of 12 mm, was sealed in a quartz ampoule under vacuum conditions of 10^{-4} Pa. Subsequently, the polycrystalline CBIB was transferred to a three-zone modified vertical Bridgman furnace. The zones differed in terms of the growth temperature, temperature gradient, crystal growth rate, and cooling rate. The temperatures in the upper, middle, and lower zones were 700-720 °C, 500-550 °C, and 400-450 °C, respectively. The ampoule was maintained in the high-temperature zone for 24 h to completely melt the polycrystalline CBIB. Subsequently, the quartz ampoule was gradually moved down to the low temperature zone. After the CBIB SC growth, the furnace temperature was reduced to room temperature (30 °C). Finally, the bulk CBIB SCs were harvested. The growth experiments of CBIB SCs are summarized in **Table S3**.

5. The EDS-mappings of $CBI_{8.3}B_{0.7}$, $CBI_{8.5}B_{0.5}$, and CBI SCs.

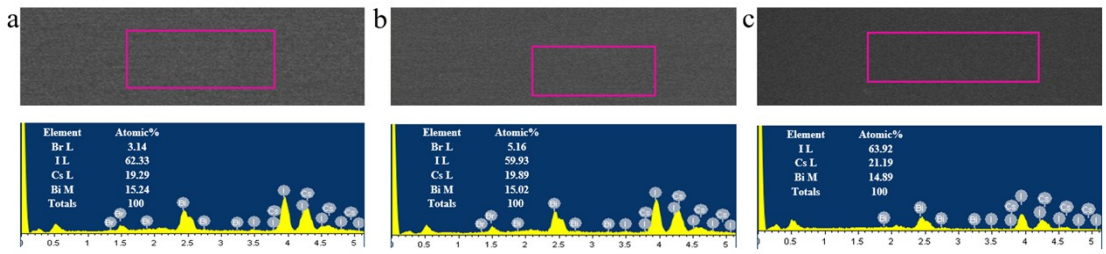

Figure S2. EDS of $CBI_{8.3}B_{0.7}$, $CBI_{8.5}B_{0.5}$, and CBI SCs.

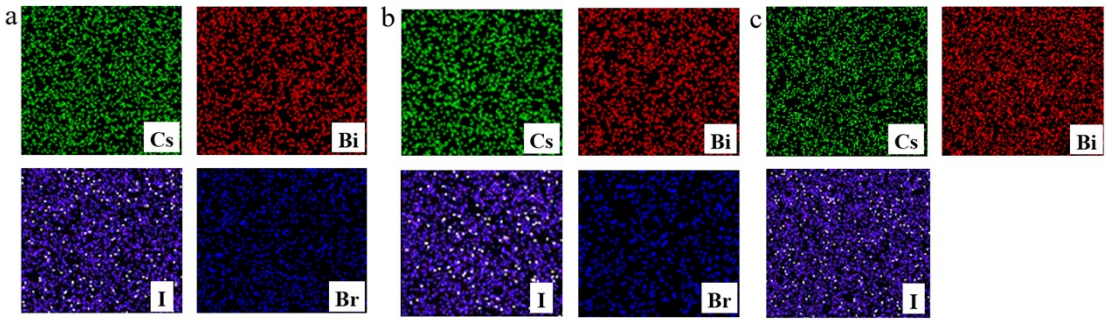

Figure S3. The EDS mappings of $CBI_{8.3}B_{0.7}$, $CBI_{8.5}B_{0.5}$, and CBI SCs.

6. The X-ray Laue back diffraction patterns of $CBI_{8.3}B_{0.7}$ SCs.

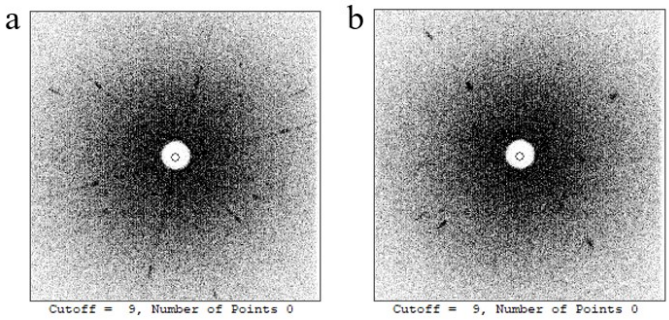

Figure S4. X-ray Laue back diffraction patterns of (a) (001) plane and (b) $(\bar{1}20)$ plane.

7. The hardness of $CBI_{8.3}B_{0.7}$ SCs.

Figure S5 shows that the indentations are obtained by pressure on the surface of (001) and $(\bar{1}20)$ planes.

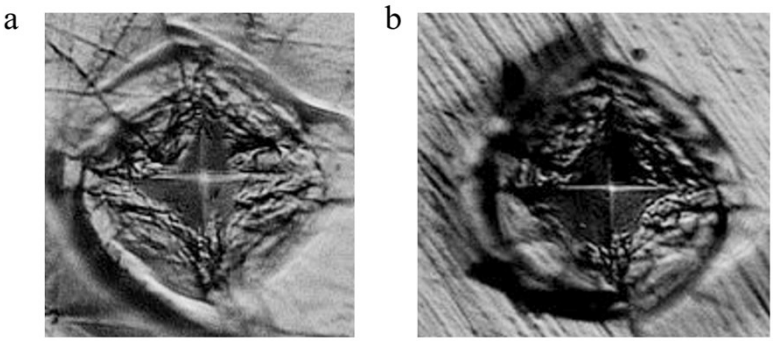

Figure S5. Photographs of the diamond square-based pyramid indentation on the (a) (001) and (b) $(\bar{1}20)$ planes.

8. The specific heat and thermal diffusivity of $CBI_{8.3}B_{0.7}$ SC.

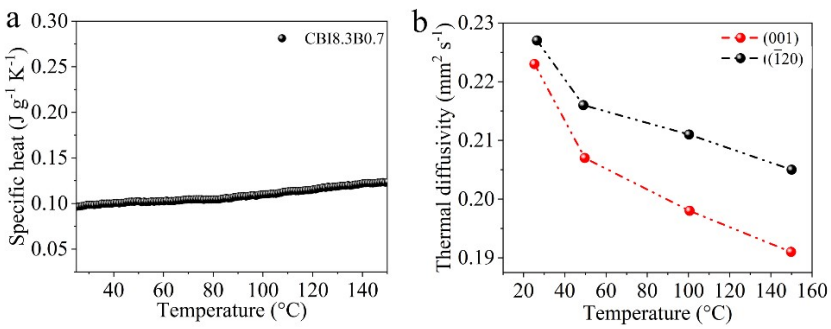

Figure S6. (a) Temperature dependence of specific heat for the $CBI_{8.3}B_{0.7}$ SC. (b) Temperature dependence of the thermal diffusivity for the $CBI_{8.3}B_{0.7}$ SC along the *b*- and *c*- axes.

9. The attenuation efficiency and 100 keV X-ray detection of $CBI_{8.3}B_{0.7}$ SC.

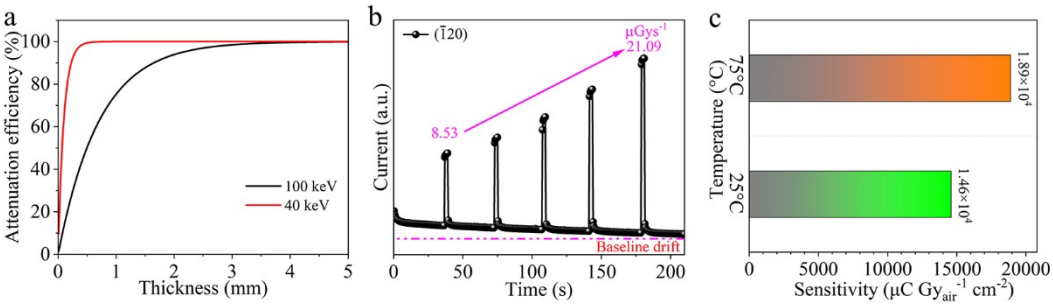

Figure S7. (a) Attenuation efficiency versus thickness of $CBI_{8.3}B_{0.7}$ for 40 and 100 keV X-ray photons. (b) Photocurrent response of $(\bar{1}20)$ plane under the electric field of 400 V mm^{-1} for 100 keV hard X-rays. (c) The sensitivity of (001) plane under the electric field of 400 V mm^{-1} at the temperature of 25 and 75 °C.

10. The 40 keV soft X-ray Detection of $CBI_{8.3}B_{0.7}$ SC.

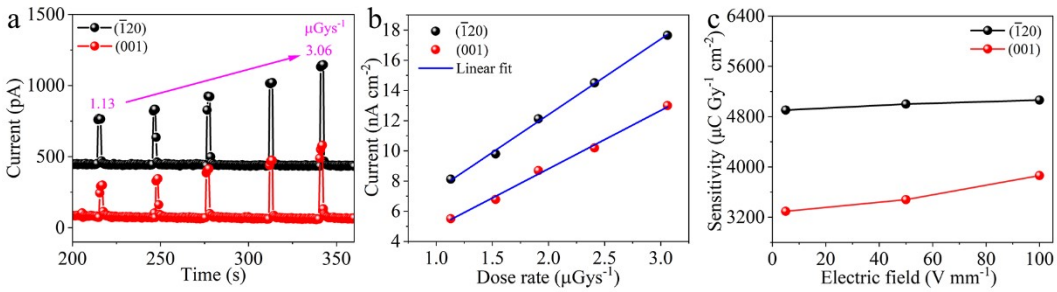

Figure S8. (a) Photocurrent response and (b) current density for (001) and $(\bar{1}20)$ planes of $CBI_{8.3}B_{0.7}$ detectors under the electric field of 100 V mm^{-1} for 40 keV X-rays. (c) X-ray sensitivities of $CBI_{8.3}B_{0.7}$ SC for 40 keV X-rays.

11. Ion activation energy measure systems.

In our measurement procedure, the *I-t* curves of Au/CBIB/Au devices, depending on the temperature, were determined using Keithley 2450 instruments.[1] Symmetric Au electrodes were sputtered on a CBIB SCs wafer surface with a gap of 100 μm. An external bias of 70 V was applied to the device to realize ion migration in the temperature-dependent transient response measurement (Charging process). Eventually, these ions accumulated at the CBIB/ Au electrode interface and reached equilibrium (Equilibrium process). Ion vacancies promptly migrated after suddenly turning off the external bias because of the large concentration gradient, forming a negative current (Discharging process). The ion activation energy was fitted using the Arrhenius function, from the *I-t* curves measured at different temperatures.

12. X-ray detection systems.

In this study, we built an X-ray generating and shielding device to characterize the X-ray detection capability of $Cs_3Bi_2I_{8.3}Br_{0.7}$ SCs.[1] During the experiment, the devices were exposed to a tungsten anode X-ray tube with a photon energy in the range of 40-150 keV, which was modulated by changing the voltage of the tube. The radiation dose rate was carefully calibrated using a Piranha 655 X-ray machine multifunctional quality detector by adjusting the current of the tube. The X-ray device consists of the VAREX RAD-14/Leo X-ray tube, Ralco R302L/A beam limiter, EMD EPS SYS 50R high-voltage generator (generating X-rays), and a lead box (shielding X-rays). Different X-ray dose rates can be obtained by adjusting the tube voltage and current of the generator. The accurate calibration of the X-ray dose rate is necessary to obtain credible results. A commercial Piranha 655 X-ray machine multifunctional quality detector was used to measure the dose rate. The X-ray radiation window size of the beam limiter was 1 × 1 mm^2, and the distance between the window and detector was 110 cm. The calibration results are listed in **Tables S4 and S5** for 40 and 100 keV X-rays. Furthermore, the X-ray dose rate was tested three times at each measurement point, and the average value was calculated to ensure the accuracy of the test.

Table S1. Dielectric constants of $CBI_{8.3}B_{0.7}$ SC.

Crystal plane	Average values
(001)	14.05
($\bar{1}$20)	13.99

Table S2. Sensitivity and low detection limit for reported perovskite-based single crystal X-ray detectors.

Structure/ Materials Single crystal	Electric Field ($V\ cm^{-1}$)	Device area (mm^2)	Photon energy (keV)	Sensitivity ($\mu C\ Gy_{air}^{-1}\ cm^{-2}$)	Low detection limit ($nGy_{air}\ s^{-1}$)	Ref
3D $MAPbI_3$	1000	-	50	700000	1.5	[2]

2D $(F\text{-}PEA)_2PbI_4$	~1333	-	120	3402	23	[3]
3D $MAPbBr_3$	61	-	120	3928	-	[4]
3D $CsPbBr_{2.9}I_{0.1}$	5000	4	120	63000	54	[5]
2D $(BDA)PbI_4$	3100	-	40	242	420	[6]
0D Cs_2TeI_6	27.6	4	40	27.8	72.5	[7]
3D $Cs_2AgBi_2Br_6$	250	3.14	50	105	59.5	[8]
2D $Rb_3Bi_2I_9$	3000	3	50	159.7	8.32	[9]
0D $FA_3Bi_2I_9$	5550	9	34.3	598	200	[10]
0D $Ag_3Bi_2I_9$	3.8	9	43	282.5	72	[11]
0D $MA_3Bi_2I_9$	600	1	40	1947	83	[12]
0D $MA_3Bi_2I_9$	~480	-	140	10620	0.62	[13]
0D $(NH_4)_3Bi_2I_9$	22	-	50	8000	55	[14]
2D $Cs_3Bi_2I_6Br_3$	3000	4	20	3195	-	[15]
0D $Cs_3Bi_2I_9$	500	1	40	1652	130	[16]
2D $Cs_3Bi_2Br_9$ (001) plane	10000	4	120	1705	0.58	[17]
	10000	4	70	978	1.22	
	10000	4	40	538	5.5	
2D $Cs_3Bi_2I_8Br$ (001) plane	4000	4	100	13299	28.64	[1]
	4000	4	70	12341	29.51	
	4000	4	40	5557	39.7	
$CBI_{8.3}B_{0.7}$ (001) plane	1000	4	100	6322	32.41	**This work**
	4000	4	100	1.46×10^4	-	
	4000	4	100	1.89×10^4 (75 °C)	-	

$CBI_{8.3}B_{0.7}$ ($\bar{1}20$) plane	1000	4	100	7579	101.85

It is significant for temperature gradient, slow growth rate, and cooling rate in crystal growth experiments. Therefore, three crystal growth experiments were performed as follows.

Table S3. CBIB single crystals grown by the modified Bridgman method with different growth parameters.

Temperature gradient	Growth rate	Cooling rate
15 °C cm^{-1}	1 mm h^{-1}	4 °C h^{-1}

Table S4. Dose rate calibration of 40 keV X-rays.

Tube current (mA)	Dose rate-1 (μGy s^{-1})	Dose rate-2 (μGy s^{-1})	Dose rate-3 (μGy s^{-1})	Averaged dose rate (μGy s^{-1})
10	1.136	1.177	1.07	1.13
12.5	1.527	1.53	1.533	1.53
16	1.943	1.977	1.814	1.91
20	2.412	2.464	2.355	2.41
25	3.085	3.148	2.951	3.06

Table S5. Dose rate calibration of 100 keV X-rays.

Tube current (mA)	Dose rate-1 (μGy s^{-1})	Dose rate-2 (μGy s^{-1})	Dose rate-3 (μGy s^{-1})	Averaged dose rate (μGy s^{-1})
10	8.504	8.541	8.532	8.53
12.5	10.5	10.67	10.58	10.58
16	13.28	13.45	13.18	13.30
20	16.79	17.1	16.8	16.90
25	20.9	21.54	20.82	21.09

References

1. X. Li, G. Zhang, Y. Hua, F. Cui, X. Sun, J. Liu, H. Liu, Y. Bi, Z. Yue, Z. Zhai, H. Xia and X. Tao, *Angewandte Chemie International Edition*, 2023, **e202315817**.
2. Y. Song, L. Li, W. Bi, M. Hao, Y. Kang, A. Wang, Z. Wang, H. Li, X. Li, Y. Fang, D. Yang and Q. Dong, *Research*, 2020, **2020**, 5958243.
3. H. Li, J. Song, W. Pan, D. Xu, W. A. Zhu, H. Wei and B. Yang, *Adv Mater*, 2020, **32**, e2003790.
4. J. Song, X. Feng, H. Li, W. Li, T. Lu, C. Guo, H. Zhang, H. Wei and B. Yang, *J Phys Chem Lett*, 2020, **11**, 3529-3535.
5. P. Zhang, Y. Hua, Y. Xu, Q. Sun, X. Li, F. Cui, L. Liu, Y. Bi, G. Zhang and X. Tao, *Adv Mater*, 2022, **34**, e2106562.
6. Y. Shen, Y. Liu, H. Ye, Y. Zheng, Q. Wei, Y. Xia, Y. Chen, K. Zhao, W. Huang and S. F. Liu, *Angew Chem Int Ed Engl*, 2020, ***59***, 14896-14902.
7. B. Xiao, F. Wang, M. Xu, X. Liu, Q. Sun, B.-B. Zhang, W. Jie, P. Sellin and Y. Xu, *CrystEngComm*, 2020, **22**, 5130-5136.
8. W. Pan, H. Wu, J. Luo, Z. Deng, C. Ge, C. Chen, X. Jiang, W.-J. Yin, G. Niu, L. Zhu, L. Yin, Y. Zhou, Q. Xie, X. Ke, M. Sui and J. Tang, *Nature Photonics*, 2017, **11**, 726-732.
9. M. Xia, J. H. Yuan, G. Niu, X. Du, L. Yin, W. Pan, J. Luo, Z. Li, H. Zhao and K. H. Xue, *Advanced Functional Materials*, 2020, 1910648.
10. W. Li, D. Xin, S. Tie, J. Ren, S. Dong, L. Lei, X. Zheng, Y. Zhao and W. H. Zhang, *J Phys Chem Lett*, 2021, **12**, 1778-1785.
11. S. Tie, W. Zhao, W. Huang, D. Xin, M. Zhang, Z. Yang, J. Long, Q. Chen, X. Zheng, J. Zhu and W. H. Zhang, *J Phys Chem Lett*, 2020, **11**, 7939-7945.
12. Y. Liu, Z. Xu, Z. Yang, Y. Zhang, J. Cui, Y. He, H. Ye, K. Zhao, H. Sun, R. Lu, M. Liu, M. G. Kanatzidis and S. Liu, *Matter*, 2020, **3**, 180-196.
13. X. Zheng, W. Zhao, P. Wang, H. Tan, M. I. Saidaminov, S. Tie, L. Chen, Y. Peng, J. Long and W.-H. Zhang, *Journal of Energy Chemistry*, 2020, **49**, 299-306.
14. R. Zhuang, X. Wang, W. Ma, Y. Wu, X. Chen, L. Tang, H. Zhu, J. Liu, L. Wu and W. Zhou, *Nature Photonics*, 2019, **13**, 602-608.
15. Q. Sun, B. Xiao, L. Ji, D. Zhao, J. Liu, W. Zhang, M. Zhu, W. Jie, B.-B. Zhang and Y. Xu, *Journal of Energy Chemistry*, 2022, **66**, 459-465.
16. Y. Zhang, Y. Liu, Z. Xu, H. Ye, Z. Yang, J. You, M. Liu, Y. He, M. G. Kanatzidis and S. F. Liu, *Nature communications*, 2020, **11**, 1-11.
17. X. Li, P. Zhang, Y. Hua, F. Cui, X. Sun, L. Liu, Y. Bi, Z. Yue, G. Zhang and X. Tao, *ACS Appl Mater Interfaces*, 2022, **14**, 9340-9351.